Nanoscale

ROYAL SOCIETY OF CHEMISTRY

PAPER

View Article Online
View Journal | View Issue

Cite this: *Nanoscale*, 2022, **14**, 1468

White light emission from lead-free mixed-cation doped Cs_2SnCl_6 nanocrystals†

Samrat Das Adhikari, *[a] Carlos Echeverría-Arrondo, [a] Rafael S. Sánchez, [a] Vladimir S. Chirvony,[b] Juan P. Martínez-Pastor, [b] Saïd Agouram,[c,d] Vicente Muñoz-Sanjosé [c,d] and Iván Mora-Seró *[a,d]

Received 22nd September 2021,
Accepted 14th December 2021

DOI: 10.1039/d1nr06255g

rsc.li/nanoscale

We have designed a synthesis procedure to obtain Cs_2SnCl_6 nanocrystals (NCs) doped with metal ion(s) to emit visible light. Cs_2SnCl_6 NCs doped with Bi^{3+}, Te^{4+} and Sb^{3+} ions emitted blue, yellow and red light, respectively. In addition, NCs simultaneously doped with Bi^{3+} and Te^{4+} ions were synthesized in a single run. Combination of both dopant ions together gives rise to the white emission. The photoluminescence quantum yields of the blue, yellow and white emissions are up to 26.5, 28, and 16.6%, respectively under excitation at 350, 390, and 370 nm. Pure white-light emission with CIE chromaticity coordinates of (0.32, 0.33) and (0.32, 0.32) at 340 and 370 nm excitation wavelength, respectively, was obtained. The as-prepared NCs were found to demonstrate a long-time stability, resistance to humidity, and an ability to be well-dispersed in polar solvents without property degradation due to their hydrophilicity, which could be of significant interest for wide application purposes.

1. Introduction

Metal halide perovskites (MHPs) and their analogues have recently emerged as new optoelectronic materials with outstanding characteristics for efficient solid state lighting applications.[1–4] MHPs have been successfully used to fabricate white-light emitting diodes (WLEDs).[5–8] There are two possibilities to provide a white-light emission from the MHP emitters: (i) use of a mixture of emitters of different colours, and (ii) use of one-type emitters with a broad photoluminescence (PL) spectrum. The former approach, which has been mostly studied for lead halide perovskites,[9] is possible for the band-to-band emitting MHP semiconductors. However, a formation of blends of solution processed nanocrystals (NCs) is limited because of the anion exchange processes and hence the formation of mixed halide NCs with a new emission.[10–13] Typically, to avoid the anion exchange and provide a white emission in a mixture of different light-emitting perovskite NCs, wrapping the perovskite NCs by silica or coating by a polymer or $PbSO_4$-oleate is used,[14–17] or mixing a MHP with another emitter of different nature that complements its emission in order to obtain a white color, for example as in case of combining with carbon quantum dots.[18] A white emission from single MHP emitters is usually provided by broadband PL from self-trapped excitons (STE), where the categorized materials are mostly 1D or 2D metal halide hybrid organic–inorganic layered perovskites,[19–23] or all-inorganic lead-free MHPs.[24–26] The white emission from single MHPs has been successfully achieved for polycrystalline thin films or NCs. Needless to say, lead-free MHPs have been studied from this point of view more intensively than their Pb-based counterparts because of their low toxicity. Among these MHPs, double halide perovskites (DHP) are a class of materials with predominantly reported STE characteristics to provide the white-light emission.[27]

The general formula of DHP is $A_2B(I)B'(III)X_6$, where $B(I)X_6$ and $B'(III)X_6$ are metal–halide octahedra alternatively corner-shared to each other with a 3D connected geometry. When one of the B-site is omitted from the crystal lattice by placing a virtually-vacant octahedra, which is apparently connected to each of the $[BX_6]$ entity, such kind of DHP is known as vacancy-ordered DHP, formulated as A_2BX_6.[27,28] Noteworthy, the oxidation state of the B-site becomes "+4". Examples of vacancy-ordered DHPs are: Cs_2SnX_6, Cs_2TeX_6, Cs_2ZrX_6, Cs_2PdX_6 *etc.* (X = Cl, Br, I), which have been experimentally reported so far according to their synthesis and optoelectronic properties. A high oxidation state of the B-site cation (+4) is beneficial for a

[a]*Institute of Advanced Materials (INAM), Universitat Jaume I. Av. de Vicent Sos Baynat, s/n 12006, Castelló de la Plana, Spain. E-mail: dasadhik@uji.es, sero@uji.es*
[b]*Instituto de Ciencia de Materiales (ICMUV), Universitat de Valencia, 46980 Paterna, Spain*
[c]*Department of Applied Physics and Electromagnetism, University of Valencia, Valencia 46100, Spain*
[d]*Materials for Renewable Energy (MAER), Unitat Mixta d'Investigació UV-UJI, Valencia 46010, Spain*

†Electronic supplementary information (ESI) available. See DOI: 10.1039/d1nr06255g

stability of these materials under ambient conditions.[29–34] Since the metal halide octahedra are not corner-shared to each other, these are from the family of 0D materials. Recently, Cs_2SnCl_6, a class of 0D vacancy-ordered DHP, has been reported with dopant-induced STE emission with Bi^{3+}, Te^{4+} and Sb^{3+} as dopants emitting blue, yellow and red photoluminescence (PL), respectively, with high PL quantum yields (PLQYs).[35–39] Doping with Bi^{3+} and Sb^{3+} has been also extensively studied for 3D DHPs to provide broadband emission for optoelectronic applications.[40–46] In a recent work Zhou *et al.* reported white-light emission from a mixture of Bi^{3+} and Sb^{3+} co-doped $Cs_2NaInCl_6$ DHP.[47] Apart from the role as dopants, Bi^{3+}, Sb^{3+} and Te^{4+} have also been successfully used as ideal B-site cations in order to provide alternative lead-free perovskite semiconductors for optoelectronic applications.[30,48,49]

So far, 0D perovskites possessing STE emission characteristics based on their transient lattice deformation upon photoexcitation have been reported.[50,51] While undoped Cs_2SnCl_6 does not possess any PL, an incorporation of a small percentage of one of the aforementioned dopants results in visible PL with high PLQY.[35,38] Several reports on their PL and down conversion electroluminescence have been published.[35,36] However, to the best of our knowledge, doped Cs_2SnCl_6 has been synthesized in the form of powder, while ligand capped colloidal NCs have been studied only for Sb^{3+}-doped Cs_2SnCl_6 among these.[52] Powder materials are inconvenient for subsequent deposition in thin films, as optoelectronic applications mostly requires. In this sense, the material synthesis in the form of NCs has an enormous advantage of allowing easy deposition of NCs forming thin films.[18,53] Alongside, these NCs demonstrated lower PLQY in comparison to their bulk phosphors, having a similar trend comparing with previously reported works.[46,52] Herein, we report the colloidal synthesis of Cs_2SnCl_6 NCs with a broad range of doping elements such as Bi^{3+}, Sb^{3+} and Te^{4+}, using a cost-effective synthesis methodology. We have chosen NCs with Bi^{3+} and Te^{4+} as dopant ions, which provide blue and yellow emission, respectively. We have also successfully synthesized white-light emitting dual-doped Cs_2SnCl_6 NCs in a one synthesis containing both of the Bi and Te dopants up to 0.8 and 2.8%, for 30 and 50% of initial loading of the Bi and Te-precursors with respect to Sn-precursors, which provide a combination of blue and yellow emissions from the individual dopant ions without any intervention of other impurity phases. Providing white light emission by mixing individual entities emitting light of different colors is difficult for lead halide perovskites, as has been reported[9] and previously commented because of the anion exchange processes between NCs of different types. In our synthesizing method, both cation dopants are incorporated together, and hence we obtain the white light emission by *in situ* synthesis. We propose a proficient light-emission application of these NCs because of their abundance and easy-to-prepare using a cost-effective methodology. Besides, these NCs demonstrated a stability on harvesting into polar solvents due to their hydrophilicity, which could be beneficial for wide application purposes.

2. Experimental section

2.1 Chemicals

Cesium acetate (99.9%, Sigma Aldrich), tin(II) acetate (Sigma Aldrich), bismuth(III) acetate (99.99%, Sigma Aldrich), tellurium(IV) oxide (99%, Sigma Aldrich), antimony(III) acetate (99.9%, Sigma Aldrich), oleic acid (90%, Sigma Aldrich), 1-octadecene (ODE; Sigma Aldrich), hydrochloric acid (HCl; ACS reagent, 37%, Sigma Aldrich), acetone, isopropanol, *N*-methyl-2-pyrrolidone.

2.2 Synthesis

2.2.1 Bismuth and antimony doped Cs_2SnCl_6 nanocrystals. In a three-necked flask, 46 mg of tin(II) acetate (0.2 mmol), 76 mg of cesium acetate (0.4 mmol), and different amounts of bismuth(III) acetate (10–50% wrt tin acetate) were loaded together along with 1 ml of oleic acid and 10 ml of ODE, and degassed under vacuum at 120 °C for 1 hour. A clear solution was obtained which confirms the formation of metal oleates, and the solution was filled with nitrogen. This whole procedure was carried out in inert condition in order to prevent the unwanted reaction under air atmosphere. The next step of the reaction was the halogenation of the metal precursor solution. The metal precursor solution was cooled down to room temperature and the solution transferred to a beaker containing 1 ml of HCl. The beaker containing HCl (in aqueous medium) and metal oleates (in organic medium) were sonicated for 10 minutes. The solution turned yellow after the addition of HCl. After that, 10 ml of acetone was added to the beaker, and stirred at room temperature for 30 minutes. Upon the addition of acetone to the solution, the solution turned white, which confirms the formation of nanocrystals. The precipitate was collected by centrifugation at 5000 rpm for 5 minutes, and washed with acetone for two times at the same centrifugation rate to remove the excess of water from HCl. Finally, the nanocrystals were dispersed in toluene or acetone.

For the preparation of antimony doped Cs_2SnCl_6 nanocrystals, the same procedure was followed. Antimony(III) acetate was taken instead of bismuth(III) acetate. The solution turned white after the HCl treatment and remained with the same white color upon the addition of acetone. The purification procedure was the same as for bismuth doped nanocrystals.

2.2.2 Tellurium(IV) doped Cs_2SnCl_6 nanocrystals. In a three-necked flask, 46 mg of tin(II) acetate (0.2 mmol) and 76 mg of cesium acetate (0.4 mmol) were loaded together along with 1 ml of oleic acid and 10 ml of ODE, and degassed under vacuum at 120 °C for 1 hour. Once a clear solution of metal precursors was observed, the reaction flask was filled with nitrogen and cooled down to room temperature. In a beaker, TeO_2 (10–50% wrt tin acetate) was dissolved in 1 ml of HCl, and the metal precursor solution was added onto it. The solution was sonicated for 10 minutes followed by the addition of acetone, and stirred for 1 hour under ambient condition. The temperature of the reaction medium was maintained at 40–50 °C. The solution turned black just after the addition of acetone, and slowly changed the color to pale yellow over an

hour. The purification procedure and the harvesting of the nanocrystals was the same as described above.

2.2.3 Dual-doped (Bi^{3+}/Te^{4+}) Cs_2SnCl_6 nanocrystals. The dual doping of bismuth and tellurium in Cs_2SnCl_6 host nanocrystals was carried out by the combination of bismuth and tellurium doping strategies. In brief, 46 mg of tin(II) acetate (0.2 mmol), 76 mg of cesium acetate (0.4 mmol), and various amounts of bismuth(III) acetate (10–50% wrt tin acetate) were loaded in a three-necked flask along with 1 ml of oleic acid and 10 ml of ODE, and degassed under vacuum at 120 °C for 1 hour. After the complete dissolution of the metal precursors, the solution was filled with nitrogen and cooled down to room temperature. In a beaker, TeO_2 (10–50% wrt tin acetate) was dissolved in 1 ml of HCl, and the metal precursor solution was added onto it. The solution was sonicated for 10 minutes followed by the addition of acetone, and stirred for 1 hour under ambient condition. The solution turned to black after the acetone treatment, and turned to faint dark yellow to dark whitish color over one hour upon maintaining the reaction medium at 40–50 °C. The precipitate was purified and harvested following the same procedure as bismuth and tellurium doped nanocrystals.

2.2.4 Undoped Cs_2SnCl_6 nanocrystals. Synthesis of undoped Cs_2SnCl_6 nanocrystals was performed following the same procedure of bismuth doped Cs_2SnCl_6 nanocrystals, without employing any dopants into the reaction medium.

2.3 Characterizations

2.3.1 Powder X-ray diffraction (XRD). XRD measurements were performed using a D8 Advance, Bruker-AXS X-ray diffractometer. The powder samples were dispersed in acetone and drop casted onto a glass slide for the XRD measurement (Cu Kα, wavelength λ = 1.5406 Å).

2.3.2 UV-Vis absorbance. UV-Vis absorption spectra were collected from PerkinElmer UV-Vis-NIR spectrophotometer using an integrated sphere unit. The samples dispersed in acetone were drop casted on top of a quartz substrate. The transmittance spectra were obtained by a conversion of absorbance A to transmittance T using the formula $T = 10^{-A}$.

2.3.3 Photoluminescence (PL), PL excitation (PLE) and photoluminescence quantum yield (PLQY) measurements. PL and PLE measurements were carried out using a Fluorolog-Horiba Spectroflurometer. PLQY measurements were carried out using Hamamatsu C9920-02 absolute PL quantum yield measurement system. The purified samples were dispersed in acetone or toluene for the PL and PLQY measurements. PLQYs of nanocrystals in film were measured by drop casting of the NC suspension on a quartz substrate of 1 cm × 1 cm size.

2.3.4 Transmission electron microscope (TEM) and high-resolution TEM (HRTEM). TEM, high resolution TEM (HRTEM) micrographs, energy dispersive X-ray analysis (EDAX), and selected area electron diffractions (SAED) were recorded with a Tecnai G2 F20 field emission gun transmission electron microscope under an acceleration voltage of 200 kV at the SCSIE facilities (University of Valencia). For TEM measurements, NCs were deposited on carbon grid substrates.

3. Results and discussion

Metal ion(s) doped Cs_2SnCl_6 NCs were synthesized by using a ligand-assisted wet chemical method. Oleic acid was used as a ligand, and 1-octadecene (ODE) as solvent. The synthesis procedure is a two-step process. For preparation of Bi^{3+}-doped (or Sb^{3+}-doped) Cs_2SnCl_6 NCs, the first step was the formation of metal oleates, by reacting Cs-acetate, Sn(II)-acetate, and Bi(III)-acetate (or Sb(III)-acetate) with oleic acid. In the second step, hydrochloric acid (HCl) was introduced to the metal–oleate solution, and the halogenation reaction took place at the interface of an organic–aqueous layer. For preparation of Te^{4+}-doped Cs_2SnCl_6, we used TeO_2 as dopant precursor, which was added to HCl for complete dissolution followed by the second step of reaction. Noteworthy, we incorporate TeO_2 into HCl instead of adding it simultaneously with the metal precursors, because TeO_2 would remain unreacted with oleic acid in the first step of reaction. The quantity of dopant precursor was varied from 10% to 50% in order to obtain the best photoluminescence for Bi and Te-dopants with respect to Sn-precursor. Dual-doped (Bi^{3+}/Te^{4+}) Cs_2SnCl_6 NCs were synthesized by the combination of Bi-doping and Te-doping strategies. Details of the reaction scheme are provided in Fig. 1a. The synthesis methodology is established as a generic method to prepare individual Bi^{3+}, Te^{4+}, and Sb^{3+} doped or dual-doped (Bi^{3+}/Te^{4+}) Cs_2SnCl_6 NCs. The as-prepared NCs were finally dispersed in acetone or toluene. Besides, the NCs were well dispersed in *N*-methylpyrrolidone (NMP) and isopropanol without any deterioration of optical properties and/or quick precipitation. Detailed synthesis method is provided in the Experimental section. A digital image of the blue, yellow, red and white photoemission of Bi^{3+}, Te^{4+}, Sb^{3+}, and dual (both the Bi^{3+} and Te^{4+}) doped Cs_2SnCl_6 nanocrystals under 365 nm UV lamp is provided in Fig. 1b. The PLQYs of the corresponding emissions were 26.5, 28, <1, and 16.6% under the excitation at 350, 390, 350, and 370 nm, respectively. While an *in situ* introduction of both Bi^{3+} and Te^{4+} dopants provided a white-light emission as a result of combination of the blue and yellow emissions from the individual dopant centers, analogous white emission was also observed when individual Bi^{3+} and Te^{4+} doped NCs were mixed post-synthetically (Fig. S1a†). Our attempt of *in situ* preparation of Sb^{3+}, Bi^{3+} and Te^{4+} triple-doped Cs_2SnCl_6 NCs failed, giving rise only to a very poor red emission. However, a post-synthetic mixing of different blue, yellow (or white) and red emissive NCs produced a warm white-light emission (Fig. S1b†). The synthesized NCs allows easy preparation of NC thin films, see Fig. 1c and d. Crystal structures of undoped Cs_2SnCl_6 and the B-site doped Cs_2SnCl_6 is provided in Fig. 1e, where the tin halide octahedra ($SnCl_6$) are not connected to other octahedra, or virtual vacant corner-shared octahedra are connected to each other. The metal–ligand coordination is octahedral for the dopant metal chlor-

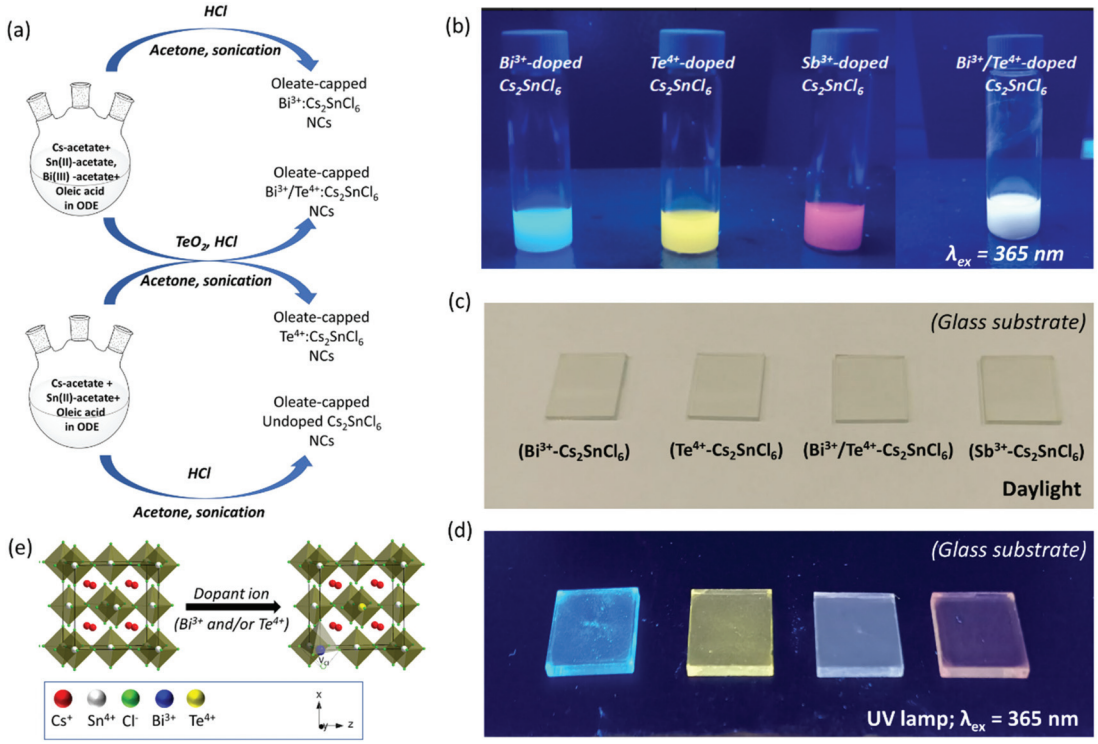

Fig. 1 (a) Schematic presentation of reaction. (b) Digital image of illuminated suspensions of NCs under a 365 nm UV-lamp. Digital images of Bi^{3+}, Te^{4+}, Bi^{3+}/Te^{4+}, and Sb^{3+}-doped Cs_2SnCl_6 NCs spin-coated on top of a glass substrate under (c) the daylight and (d) a 365 nm UV-lamp. (e) Crystal structure model of Cs_2SnCl_6, and the corresponding dopant substitution model.

ides, except Bi. The coordination of Bi-dopant consists of $[BiCl_5]$ pyramidal entity plus a Cl vacant substituting the $[SnCl_6]$ octahedra. The geometry of the Bi–Cl coordination is predicted from a detailed theoretical calculation from a literature report.[35]

The UV-Vis absorbance spectra of purified Bi^{3+}, Te^{4+} and Sb^{3+} doped Cs_2SnCl_6 NCs are presented in Fig. 2a, b, and S2a,† respectively. Bi^{3+} and Sb^{3+} doped NCs have deep UV absorption band with a maximum near 340 nm, while Te^{4+} doped NCs have a double-peak absorption, one peak in the UV region near 300–340 nm, and another one in the near-UV to visible region 380–425 nm. Their characteristic blue, yellow and red photoluminescence (PL), 1-T (where T is transmittance) and PL excitation (PLE) spectra are presented in Fig. 2c, d and S2b.† We optimized the dopant percentage at 30% of Bi-precursor for the blue-emitter, and 50% of Te-precursor for the yellow-emitter, which provides highest PL intensity, beyond which the PL intensity was nearly saturated. Fig. S3a, b and Tables S1 and S2† provides the PL spectra and PLQYs of Bi^{3+} and Te^{4+} doped Cs_2SnCl_6 NCs at different dopant precursor concentrations. The origin of these emissions is from STEs, which is supported by large Stokes shifts and broad emission bandwidths (Table 1). For PL measurements, Bi^{3+}- and Sb^{3+}-doped Cs_2SnCl_6 NCs were excited at 350 nm, and Te^{4+}-doped Cs_2SnCl_6 NCs were excited at 390 nm. Detailed optical characteristics including absolute PLQYs data are provided in Table 1. These experiments were carried out with NCs dispersed in toluene (or acetone).

Beyond the doping with a single dopant, simultaneous doping with two ions was performed. The synthesis was carried out *in situ* with the aim of incorporating both the Bi^{3+} and Te^{4+} dopants into Cs_2SnCl_6 NCs. Herein, we obtained an aggregated white emission from the mixture of blue and yellow emitters. Interestingly, we were able to acquire the white light emission from the one pot reaction of dual-doped (Bi^{3+} and Te^{4+}) Cs_2SnCl_6 NCs, where no other phase mixing was observed. We optimized the best obtained white-emission from the initial loading of the 30% of Bi-dopant and 50% of Te-dopant precursors. Optical characteristics of white emitting dual-doped Bi/Te-Cs_2SnCl_6 NCs are presented in Fig. 3. Fig. 3a presents the PL, 1-T, and PLE spectra of white emissive dual-doped Cs_2SnCl_6 NCs. Two different PLE spectra corresponding to PL emissions at 450 nm (blue line) and 570 nm (green line) are presented, corresponding to the PL peak positions produced by Bi^{3+} and Te^{4+} dopants, respectively. The overlapping of two PLE spectra determines common excitation spectral region suitable to generate the white light emission (Fig. S4†). The suitable excitation wavelengths in this region for obtaining maximum white emission are found to be at ~340 and 370 nm. The PLE spectrum detected at 500 nm, a wavelength common for both Bi^{3+} and Te^{4+} dopant emissions, includes features from both of the dopant centers (Fig. S5†). A variation of Bi and Te-precursor concentrations was carried out to optimize the best white-emission, and their PL spectra are presented in Fig. S6,† and corresponding PLQYs in Table S3.† Fig. S7† presents the UV-Vis absorbance of dual-doped Cs_2SnCl_6

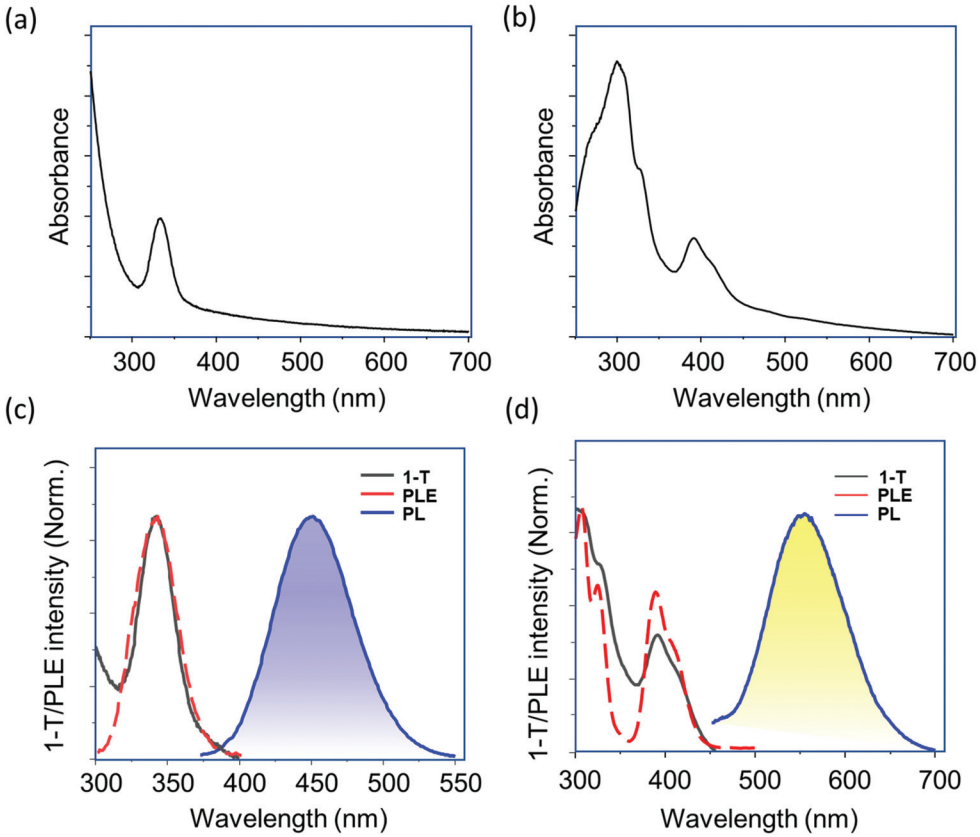

Fig. 2 UV-Vis absorbance of (a) Bi^{3+}-doped and (b) Te^{4+}-doped Cs_2SnCl_6 NCs. PL, PLE and 1-T spectra of (c) Bi^{3+}-doped and (d) Te^{4+}-doped Cs_2SnCl_6 NCs. The excitation wavelength for the blue emission was 350 nm, and 390 nm for the yellow emission. Details of the optical properties are provided in Table 1.

Table 1 Optical characteristics of different metal-ion doped Cs_2SnCl_6 NCs obtained from our synthesis protocol

Dopant ion	Excitation wavelength (nm)	PL maximum (nm)	Stokes shift (nm)	FWHM of emission peak (nm)	PLQY (%) *(in solution)*	Light emission under the UV lamp (365 nm)
Bi^{3+}	350	450	108	80	26.5	Blue
Te^{4+}	390	570	160	105	28	Yellow
Sb^{3+}	350	650	290	180	<1	Red

NCs, which includes the absorption features from both the dopants. Fig. 3b presents a set of PL spectra measured under different excitation wavelength. A ratio of intensities at the maximum points of yellow *versus* blue emission calculated from Fig. 3b and plotted against excitation wavelength is presented in Fig. 3c, where equal intensities of both the blue and yellow PL, well suited for white emission, comes at ~340 and 370 nm excitation, with PYQY of 10.6 and 16.6%, respectively. A plot of PLQY *versus* excitation wavelength is presented in Fig. S8† and shows that PLQY decreased from 340 to 345 nm due to a growth of the blue PL contribution and increases beyond 350 nm due to a growth of the yellow PL contribution. Noteworthy, individual blue-emitting Bi^{3+} doped Cs_2SnCl_6 NCs possessed a PLQY ~26.5% at the excitation wavelength of 350 nm, and the yellow-emitting Te^{4+}-doped Cs_2SnCl_6 possessed a PLQY of ~28% at the excitation wavelength of 390 nm, while dual doped Cs_2SnCl_6 NCs presents a maximum PLQY of ~18.37%, for an excitation wavelength of 375 nm. When these two ions were doped *in situ*, it resulted in lower PLQY values, which is possibly due to the reabsorption of some blue light by the yellow emitters. A CIE chromaticity coordinates of the emission spectra (presented in Fig. 3b) are presented in Fig. 3d. At 340 and 370 nm, it has a coordinate value (0.32, 0.33) and (0.32, 0.32), respectively. Table S3† provides the CIE coordinate values at different Bi and Te dopant percentages at 340 nm excitation from the PL spectra of Fig. S6.† Table S4† provides the coordinate values and correlated color temperature (CCT) values under different excitation wavelengths. At 340 and 370 nm excitation wavelengths, the CCT values are 6113 K and 6160 K, which has a good agreement with the pure white emission. Fig. 3e presents the CIE chromaticity coordinates from the blue, white and yellow emitting NCs in a same plot.

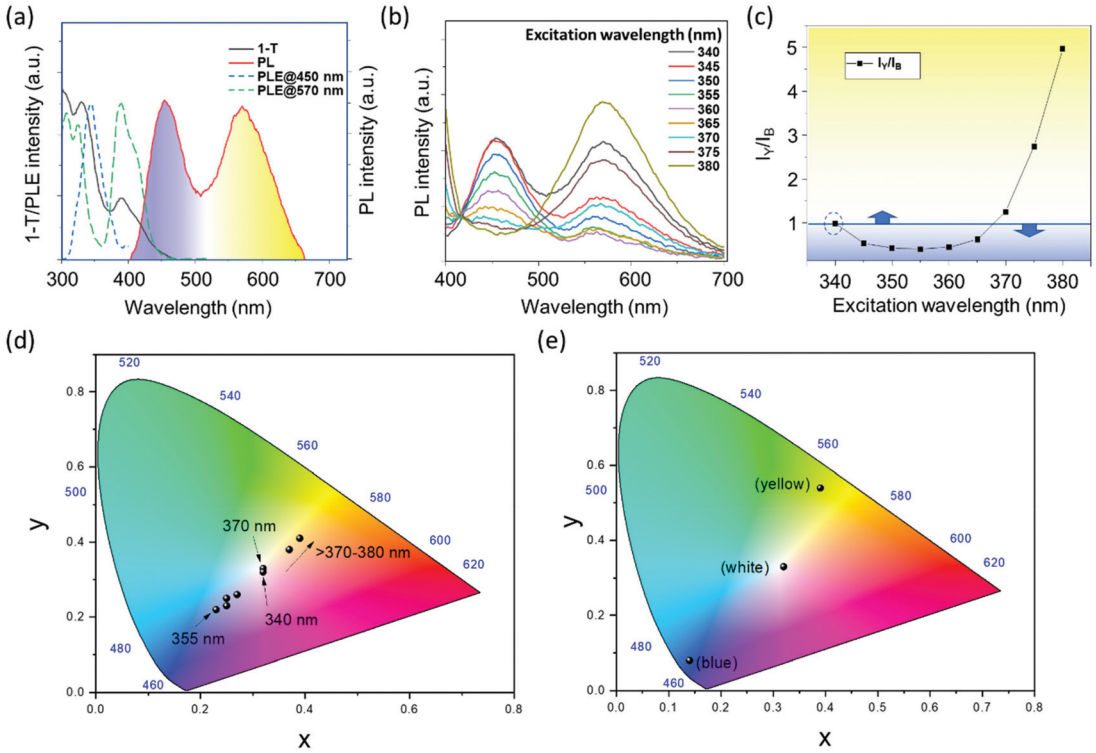

Fig. 3 (a) PL, PLE and 1-T spectra of Bi^{3+}/Te^{4+} dual doped Cs_2SnCl_6 NCs. The excitation wavelength for the PL measurement was 340 nm. PLE spectra were detected at two different emission maximum, 450 nm and 570 nm. (b) A set of PL spectra of dual-doped Cs_2SnCl_6 NCs under different excitation wavelengths. (c) Plot of peak intensity ratio of yellow/blue bands *vs.* the excitation wavelength. (d) CIE chromaticity coordinates (CIE 1931) of dual doped (Bi^{3+} and Te^{4+})-Cs_2SnCl_6 NCs. (e) CIE chromaticity coordinates (CIE 1931) of blue-emitting Bi^{3+} doped Cs_2SnCl_6 NCs (0.14, 0.08), white-emitting Bi^{3+} and Te^{4+}-doped Cs_2SnCl_6 (0.32, 0.33) and yellow-emitting Te^{4+}-doped Cs_2SnCl_6 (0.39, 0.54) NCs. Corresponding coordinate values and color temperature values are provided in Table S4.†

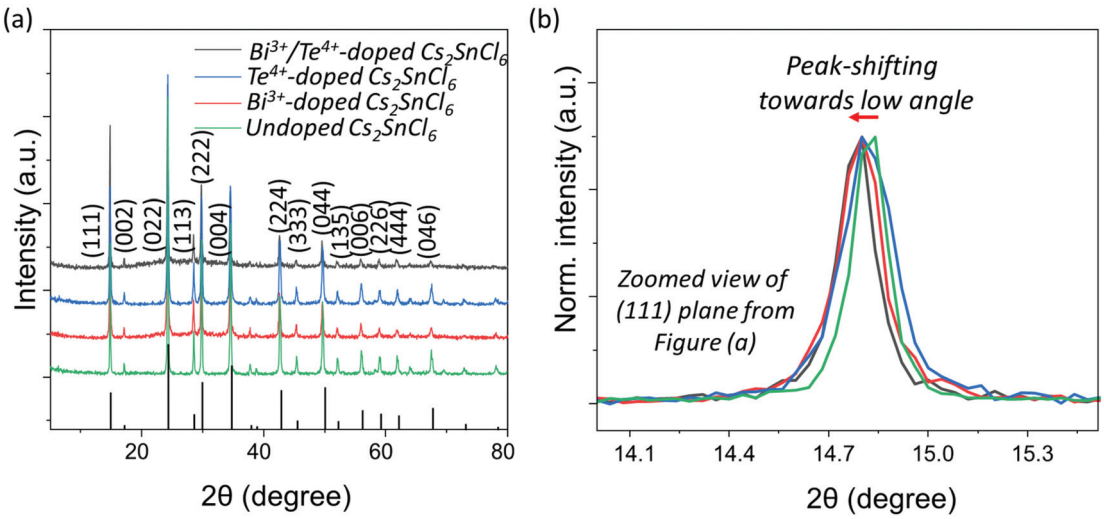

Fig. 4 (a) XRD patterns of doped and undoped Cs_2SnCl_6 NCs. The label of the XRD patterns matched with standard Cs_2SnCl_6 (COD: 1010176). (b) Zoomed XRD patterns of (111) peak extracted from Figure 4a and displaying the peak shifting for doped materials towards lower angle as compared to undoped one.

Fig. 4a displays a set of XRD patterns of Bi^{3+}, Te^{4+}, dual-doped (Bi^{3+} and Te^{4+}) and undoped Cs_2SnCl_6 NCs matched with Cs_2SnCl_6 crystal phase with COD: 1010176. These as-obtained patterns perfectly confirm the formation of phase-pure Cs_2SnCl_6 NCs using our generic synthesis method without any dopant-based additional impurity phases. Similar

XRD pattern of Sb^{3+}-doped Cs_2SnCl_6 NCs is provided in Fig. S9,† compared with the undoped Cs_2SnCl_6 and matched with the label of aforementioned Cs_2SnCl_6 crystal phase. Fig. 4b presents the zoomed XRD patterns of (111) peak extracted from Fig. 4a, which shows a XRD peak shifting towards lower angles. Basically, the shifting originates herein due to the dopant ion induced lattice expansion. A larger shift was observed in case of Bi^{3+}-doped and Bi^{3+}/Te^{4+}-doped Cs_2SnCl_6 NCs due to the larger ionic radius of Bi^{3+}, lesser shift is observed for Te^{4+}-doped Cs_2SnCl_6 NCs. Transmission electron microscopy (TEM) images of as-prepared Bi^{3+}-doped Cs_2SnCl_6, Te^{4+}-doped Cs_2SnCl_6, and Bi^{3+}/Te^{4+}-doped Cs_2SnCl_6 are provided in Fig. 5a, c, and e, respectively. TEM images of Sb^{3+}-doped Cs_2SnCl_6 and undoped Cs_2SnCl_6 NCs are provided in Fig. S10a and b.† The average particle sizes of Bi^{3+}-doped Cs_2SnCl_6, Te^{4+}-doped Cs_2SnCl_6 and dual-doped (Bi^{3+} and Te^{4+}) Cs_2SnCl_6 are between 50–70 nm.

Table 2 provides the ionic radii of different B-site cations as well as the calculated *d*-spacings from the HRTEM analysis, from which it was anticipated that incorporation of dopants will lead to the lattice expansion, which caused (i) shifting to lower angles in the XRD patterns, as observed in Fig. 4b, and (ii) increasing the *d*-spacing. HRTEM analysis of different doped- and undoped-Cs_2SnCl_6 has been made in order to determine the *d*-spacing, as pointed out in Table 2. Fig. 5b, d and f provide the HRTEM images, and the FFT with spots from the (111) plane are shown in the inset of HRTEM images. The HRTEM images of Sb^{3+}-doped Cs_2SnCl_6 and undoped

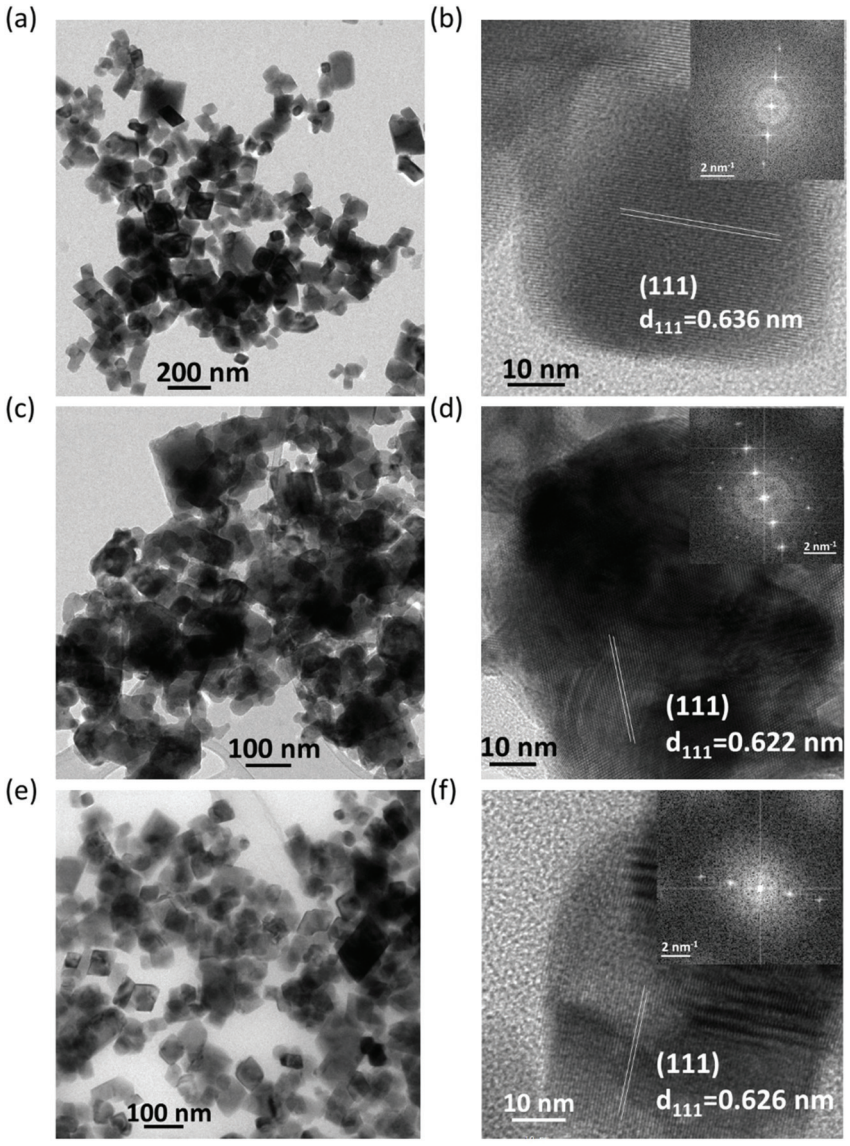

Fig. 5 (a, c and e) TEM, (b, d and f) HRTEM, and FT-SAED pattern (inset of b, d and f) of Bi^{3+}-doped (a and b), Te^{4+}-doped (c and d), and dual doped (e and f) Cs_2SnCl_6 NCs. Calculated *d*-spacings of (111) plane are mentioned in figures (b, d and f). Details of the calculated *d*-spacings are provided in Table 2.

Table 2 Ionic radius and calculated *d*-spacing from the HRTEM analysis

Material	B-site dopant/cation	Ionic radius (Å)	Calculated *d*-spacing (nm)
Bi-Doped Cs_2SnCl_6	Bi^{3+}	0.96 (5-coordination)	0.636
Te-Doped Cs_2SnCl_6	Te^{4+}	0.97 (6-coordination)	0.622
Dual-doped Cs_2SnCl_6	Bi^{3+}/Te^{4+}	0.96/0.97	0.626
Sb-Doped Cs_2SnCl_6	Sb^{3+}	0.76 (6-coordination)	0.618
Undoped Cs_2SnCl_6	Sn^{4+}	0.69 (6-coordination)	0.605

Cs_2SnCl_6 NCs and the FFT with the spots from the (111) plane are shown in Fig. S11a and b.† The elemental composition was estimated using the energy dispersive spectroscopic (EDS) analysis (Tables S5–S9†), obtaining a Bi^{3+}-doping of 0.6–1%, and a Te^{4+}-doping of 2.8% with an initial loading of 30% of Bi and 50% of Te-dopant precursors. For dual-doped (Bi^{3+} and Te^{4+}) Cs_2SnCl_6 NCs, intake of 30% of Bi-dopant and 50% of Te-dopant precursors finally retained nearly up to 0.8% of Bi^{3+}, and 2.8% of Te^{4+} in the white-emitting dual-doped (Bi^{3+}/Te^{4+}) Cs_2SnCl_6 NCs. Hence, incorporation of little amounts of foreign dopant ions (Bi^{3+} and Te^{4+}, herein) at the B-site of Cs_2SnCl_6 NCs influence moderate-to-high dopant emission. Table S10† provides details of the dopant precursor intake into the reaction and the dopant ion percentage into the doped NCs.

Purified doped NCs show excellent stability over 40 days in the form of NCs film as well as in solution as per the laboratory reports. For stability experiments of the NCs film, the NC suspensions were spin-coated on top of a quartz glass substrate and their PL spectra were measured timewise. Fig. S12a–c and 13a–c† provide the PL data of Bi^{3+}-, Te^{4+}-, and Bi^{3+}/Te^{4+}-doped Cs_2SnCl_6 NCs spin-coated on top of a quartz-substrate, and nanocrystals suspension (in acetone) support the assertion about the stability under ambient conditions. Tables S11 and S12† provides the PLQY value of these presented PL spectra which were measured timewise. The as-prepared NCs demonstrated stability in different polar solvents like NMP, isopropanol *etc*. A photograph of illuminated dispersions of doped NCs in isopropanol is provided in Fig. S14.† Notably, these NCs possess a polar surface which provides the NCs suspension in polar solvents. Basically, the metal ions (Cs^+, Sn^{4+}, Bi^{3+}, Te^{4+}, Sb^{3+}) on surface of these nanocrystals are capped with oleic acid by the carboxylate functional group, keeping the nonpolar end outside whereas the halides (chlorides) are absolutely ligand-free. The relative concentration of halide atoms is higher in 0D A_2BX_6 in comparison to the well-known 3D counterparts with the formula ABX_3, therefore chloride atoms on the NC surface result in the surface polar character. In case of colloidally synthesized hydrophobic NCs, ligand exchange reactions are carried out post-synthetically to provide to NCs the hydrophilicity in order to disperse them into polar solvents for catalytic applications.[54] However, providing the hydrophilicity to the metal halide perovskite NCs are still elusive. Our as-synthesized hydrophilic perovskite NCs could be one of the interests in future for the catalytic applications.

We have incorporated the white-emitting NCs into PMMA with the aim of preparing a composite polymeric film, which allows controlling the loading of the optically active material and serving as a flexible substrate, for broadening the material's versatility in case the ultimate application demands specific requirements. As shown in Fig. S15,† the composite film displays a cold-white emission, resulting from a higher blue and less yellow contribution, upon excitation with 355 nm pulsed light. Thereby, this material could be potentially used, on one hand, as a down-converter by integrating it on an LED chip with emission comprised within 340 and 370 nm to provide a white-light emission, but on the other hand, it could be also exploited as a (bio-)marker or anti-counterfeiting purposes. It is worth mentioning that the small diameter of the NCs is compatible for their deposition by means of printing techniques, *e.g.* inkjet upon ink formulation and/or 3D-printing once incorporated into liquid resins or plastic filaments, for the development of advanced materials.

For understanding optical PLE and absorption spectra, we performed theoretical calculations of the bulk Bi^{3+}/Te^{4+}-doped Cs_2SnCl_6; we used for this purpose "Quantum Espresso", a computational tool based on density functional theory (DFT), plane waves, and pseudopotentials.[55] With this program, running on a high-performance computer, we have calculated an orthorhombic unit cell of 143 atoms and orthogonal dimensions 10.78 Å, 21.66 Å, and 21.51 Å. The supercell contains the host vacancy-ordered double perovskite, a Bi atom substituting a Sn atom, a Cl vacancy aside (to produce a Bi_{Sn} + V_{Cl} defect complex and a $[BiCl_5]^{2-}$ octahedron),[35] and a Te atom substituting another Sn atom (this defect gives $[TeCl_6]^{2-}$ octahedrons); the unit cell is drawn in Fig. 6a with indication of point defects. The calculations were performed on the Γ point, using Optimized Norm-Conserving Vanderbilt Pseudopotentials (ONCVPSP) generated with the generalized gradient approximation of Perdew–Burke–Ernzerhof (PBE),[56] and spin–orbit interactions. As simulation of a system with a low doping level as the case analyzed here, see Table S10,† requires a significantly long computational time, we consider theoretically a system with higher concentration to decrease the time but obtaining a representative qualitative picture of the density of states created by the doping elements.

Within this *ab initio* approach, we investigated the lowest-energy optical transitions in the crystal from the valence band into the conduction band based on the calculated densities of states, plotted in Fig. 6a. As concerns these excitations, three selection rules should be considered (set out in the ESI†).

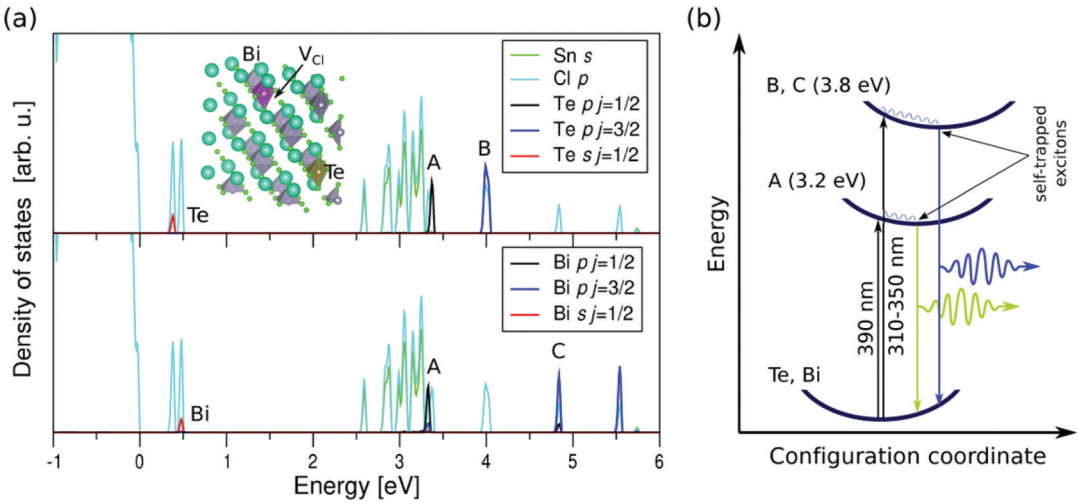

Fig. 6 (a) Bi^{3+}/Te^{4+} dual-doped Cs_2SnCl_6 supercell and projected densities of states with indication of the available levels for optical transitions, which are mostly contributed by the dopants Te and Bi, *sp*-like states appear in the peaks labeled as Te and Bi, and the *p*-like empty states are located in the peaks labeled as A, B, and C. (b) Configuration coordinate diagram illustrating absorption and emission processes indicating large Stokes shifts due to the great lattice and crystal field distortions produced by the self-trapped excitons. The wavy curves represent phonon-mediated relaxations.

Following these restrictions, the optical transitions in our material would occur between *sp*-like impurity levels localized within the band gap, and p-like empty levels in the conduction band, also contributed by the dopants (see the ESI† for more detail upon these excitations).

In Fig. 6a, the referred *sp*-like states appear in the peaks labeled as Te and Bi, and the *p*-like empty states are located in the peaks labeled as A, B, and C. The photoexcitation energies extracted from the positions of these peaks qualitatively match and theoretically explain the main experimental peaks observed in PLE and absorption spectra.

Concerning the observed PL spectra, it is worth mentioning that, when the carriers are photo-excited, they produce large distortions in the lattice resulting in a decrease of the exciton energy and therefore its trapping and spatial localization. For this reason, the localized excitations are called self-trapped excitons, which are indeed typically observed in vacancy-ordered double perovskites.[39] These photoinduced distortions result in lowering the energies of both STE-type excited states, see blue wavy lines in Fig. 6b, and thus are responsible for the large Stokes shifts observed in our PL measurements.

4. Conclusion

In summary, a generic synthesis strategy has been developed in order to synthesize ligand-capped metal ion(s) doped Cs_2SnCl_6 NCs that easily can be deposited in thin films. Bi^{3+}, Te^{4+}, and Sb^{3+} were used as the B-site dopants, which provided the blue, yellow and red emissions, respectively. As an alternative to the visible light emitting lead-halide perovskites, these materials successfully take over the visible emission coverage. As far as we know, this is the first report where Bi^{3+} and Te^{4+} doped Cs_2SnCl_6 materials have been synthesized as colloidal NCs with organic capping contrary to previous reports where bulk powders were produced. An *in situ* synthesis or the post synthetic mixing endowed the white-light emission, in which a perfect color mixing of blue and yellow emissions was realized originating from Bi and Te dopants. The CIE chromaticity coordinates support the emission of pure white PL from this material. XRD patterns of the synthesized NCs endorsed the formation of phase-pure doped and undoped Cs_2SnCl_6 NCs. The dopant inclusion was assessed by the XRD peak-shifting due to the lattice expansion caused by the replacement of Sn^{4+} with the larger sized dopant ions. The NC form allows the easy preparation of thin films by spin coating and, most important, these NC thin films were stable at least over 40 days as per the laboratory reports. Theoretical calculations revealed the incorporation of dopant ions into the Cs_2SnCl_6 matrix at the Sn-site, explaining the absorption properties and STE character of emission. In addition, NCs were dispersed in various polar solvents like isopropanol and NMP without any deterioration of optical properties due to their hydrophilicity, which could be of significant interest for wide applicability.

Conflicts of interest

There are no conflicts to declare.

Acknowledgements

This project has been partially supported by European Union's Horizon 2020 Research and Innovation Program under grant agreement no 862656 (project DROP-IT), Ministry of Science and Innovation of Spain under Project STABLE (PID2019-

107314RB-I00, PID2020-114796RB-C22), Ministry of Economy and Competitiveness of Spain (MINECO-FEDER) under Project TEC2017-85912-C2 and Generalitat Valenciana *via* Prometeo Grant Q-Devices (Prometeo/2018/098, PROMETEO/2021/066), We acknowledge SCIC from Jaume I University (UJI) for help with XRD characterization. We acknowledge the SCSIE from the University of Valencia for providing TEM facilities.

References

1 S. Adjokatse, H.-H. Fang and M. A. Loi, Broadly tunable metal halide perovskites for solid-state light-emission applications, *Mater. Today*, 2017, **20**(8), 413–424.
2 X.-K. Liu, W. Xu, S. Bai, Y. Jin, J. Wang, R. H. Friend and F. Gao, Metal halide perovskites for light-emitting diodes, *Nat. Mater.*, 2021, **20**(1), 10–21.
3 L. N. Quan, B. P. Rand, R. H. Friend, S. G. Mhaisalkar, T.-W. Lee and E. H. Sargent, Perovskites for Next-Generation Optical Sources, *Chem. Rev.*, 2019, **119**(12), 7444–7477.
4 S. D. Stranks, R. L. Z. Hoye, D. Di, R. H. Friend and F. Deschler, The Physics of Light Emission in Halide Perovskite Devices, *Adv. Mater.*, 2019, **31**(47), 1803336.
5 S. Pathak, N. Sakai, F. Wisnivesky Rocca Rivarola, S. D. Stranks, J. Liu, G. E. Eperon, C. Ducati, K. Wojciechowski, J. T. Griffiths, A. A. Haghighirad, A. Pellaroque, R. H. Friend and H. J. Snaith, Perovskite Crystals for Tunable White Light Emission, *Chem. Mater.*, 2015, **27**(23), 8066–8075.
6 D. Manna, T. K. Das and A. Yella, Tunable and Stable White Light Emission in Bi3+-Alloyed Cs2AgInCl6 Double Perovskite Nanocrystals, *Chem. Mater.*, 2019, **31**(24), 10063–10070.
7 G. Lozano, The Role of Metal Halide Perovskites in Next-Generation Lighting Devices, *J. Phys. Chem. Lett.*, 2018, **9**(14), 3987–3997.
8 K. Thirumal, W. K. Chong, W. Xie, R. Ganguly, S. K. Muduli, M. Sherburne, M. Asta, S. Mhaisalkar, T. C. Sum, H. S. Soo and N. Mathews, Morphology-Independent Stable White-Light Emission from Self-Assembled Two-Dimensional Perovskites Driven by Strong Exciton–Phonon Coupling to the Organic Framework, *Chem. Mater.*, 2017, **29**(9), 3947–3953.
9 X. Li, Y. Wu, S. Zhang, B. Cai, Y. Gu, J. Song and H. Zeng, CsPbX3 Quantum Dots for Lighting and Displays: Room-Temperature Synthesis, Photoluminescence Superiorities, Underlying Origins and White Light-Emitting Diodes, *Adv. Funct. Mater.*, 2016, **26**(15), 2435–2445.
10 G. Nedelcu, L. Protesescu, S. Yakunin, M. I. Bodnarchuk, M. J. Grotevent and M. V. Kovalenko, Fast Anion-Exchange in Highly Luminescent Nanocrystals of Cesium Lead Halide Perovskites (CsPbX3, X=Cl, Br, I), *Nano Lett.*, 2015, **15**(8), 5635–5640.
11 G. Li, J. Y.-L. Ho, M. Wong and H. S. Kwok, Reversible Anion Exchange Reaction in Solid Halide Perovskites and Its Implication in Photovoltaics, *J. Phys. Chem. C*, 2015, **119**(48), 26883–26888.
12 V. K. Ravi, R. A. Scheidt, A. Nag, M. Kuno and P. V. Kamat, To Exchange or Not to Exchange. Suppressing Anion Exchange in Cesium Lead Halide Perovskites with PbSO4−Oleate Capping, *ACS Energy Lett.*, 2018, **3**(4), 1049–1055.
13 A. F. Gualdrón-Reyes, S. J. Yoon and I. Mora-Seró, Recent insights for achieving mixed halide perovskites without halide segregation, *Curr. Opin. Electrochem.*, 2018, **11**, 84–90.
14 W. Chen, T. Shi, J. Du, Z. Zang, Z. Yao, M. Li, K. Sun, W. Hu, Y. Leng and X. Tang, Highly Stable Silica-Wrapped Mn-Doped CsPbCl3 Quantum Dots for Bright White Light-Emitting Devices, *ACS Appl. Mater. Interfaces*, 2018, **10**(50), 43978–43986.
15 L. Zhu, C. Wu, S. Riaz and J. Dai, Stable silica coated DDAB-CsPbX3 quantum dots and their application for white light-emitting diodes, *J. Lumin.*, 2021, **233**, 117884.
16 T. Xuan, J. Huang, H. Liu, S. Lou, L. Cao, W. Gan, R.-S. Liu and J. Wang, Super-Hydrophobic Cesium Lead Halide Perovskite Quantum Dot-Polymer Composites with High Stability and Luminescent Efficiency for Wide Color Gamut White Light-Emitting Diodes, *Chem. Mater.*, 2019, **31**(3), 1042–1047.
17 V. K. Ravi, R. A. Scheidt, J. DuBose and P. V. Kamat, Hierarchical Arrays of Cesium Lead Halide Perovskite Nanocrystals through Electrophoretic Deposition, *J. Am. Chem. Soc.*, 2018, **140**(28), 8887–8894.
18 R. R. Rad, A. F. Gualdrón-Reyes, S. Masi, B. A. Ganji, N. Taghavinia, S. Gené-Marimon, E. Palomares and I. Mora-Seró, Tunable Carbon–CsPbI3 Quantum Dots for White LEDs, *Adv. Opt. Mater.*, 2021, **9**(4), 2001508.
19 E. R. Dohner, A. Jaffe, L. R. Bradshaw and H. I. Karunadasa, Intrinsic White-Light Emission from Layered Hybrid Perovskites, *J. Am. Chem. Soc.*, 2014, **136**(38), 13154–13157.
20 X. Li, X. Lian, J. Pang, B. Luo, Y. Xiao, M.-D. Li, X.-C. Huang and J. Z. Zhang, Defect-Related Broadband Emission in Two-Dimensional Lead Bromide Perovskite Microsheets, *J. Phys. Chem. Lett.*, 2020, **11**(19), 8157–8163.
21 M. D. Smith and H. I. Karunadasa, White-Light Emission from Layered Halide Perovskites, *Acc. Chem. Res.*, 2018, **51**(3), 619–627.
22 Z. Yuan, C. Zhou, Y. Tian, Y. Shu, J. Messier, J. C. Wang, L. J. van de Burgt, K. Kountouriotis, Y. Xin, E. Holt, K. Schanze, R. Clark, T. Siegrist and B. Ma, One-dimensional organic lead halide perovskites with efficient bluish white-light emission, *Nat. Commun.*, 2017, **8**(1), 14051.
23 F. Liu, T. Zhang, D. Mondal, S. Teng, Y. Zhang, K. Huang, D. Wang, W. Yang, P. Mahadevan, Y. S. Zhao, R. Xie and N. Pradhan, Light-Emitting Metal–Organic Halide 1D and 2D Structures: Near-Unity Quantum Efficiency, Low-Loss Optical Waveguide and Highly Polarized Emission, *Angew. Chem., Int. Ed.*, 2021, **60**(24), 13548–13553.

24 J. Luo, M. Hu, G. Niu and J. Tang, Lead-Free Halide Perovskites and Perovskite Variants as Phosphors toward Light-Emitting Applications, *ACS Appl. Mater. Interfaces*, 2019, **11**(35), 31575–31584.

25 M. Worku, L.-J. Xu, M. Chaaban, A. Ben-Akacha and B. Ma, Optically pumped white light-emitting diodes based on metal halide perovskites and perovskite-related materials, *APL Mater.*, 2020, **8**(1), 010902.

26 J. Luo, X. Wang, S. Li, J. Liu, Y. Guo, G. Niu, L. Yao, Y. Fu, L. Gao, Q. Dong, C. Zhao, M. Leng, F. Ma, W. Liang, L. Wang, S. Jin, J. Han, L. Zhang, J. Etheridge, J. Wang, Y. Yan, E. H. Sargent and J. Tang, Efficient and stable emission of warm-white light from lead-free halide double perovskites, *Nature*, 2018, **563**(7732), 541–545.

27 A. E. Maughan, A. M. Ganose, D. O. Scanlon and J. R. Neilson, Perspectives and Design Principles of Vacancy-Ordered Double Perovskite Halide Semiconductors, *Chem. Mater.*, 2019, **31**(4), 1184–1195.

28 E. López-Fraguas, S. Masi and I. Mora-Seró, Optical Characterization of Lead-Free Cs2SnI6 Double Perovskite Fabricated from Degraded and Reconstructed CsSnI3 Films, *ACS Appl. Energy Mater.*, 2019, **2**(12), 8381–8387.

29 X. Han, J. Liang, J.-H. Yang, K. Soni, Q. Fang, W. Wang, J. Zhang, S. Jia, A. A. Martí, Y. Zhao and J. Lou, Lead-Free Double Perovskite Cs2SnX6: Facile Solution Synthesis and Excellent Stability, *Small*, 2019, **15**(39), 1901650.

30 I. Vázquez-Fernández, S. Mariotti, O. S. Hutter, M. Birkett, T. D. Veal, T. D. C. Hobson, L. J. Phillips, L. Danos, P. K. Nayak, H. J. Snaith, W. Xie, M. P. Sherburne, M. Asta and K. Durose, Vacancy-Ordered Double Perovskite Cs2TeI6 Thin Films for Optoelectronics, *Chem. Mater.*, 2020, **32**(15), 6676–6684.

31 E. Y. Peresh, O. V. Zubaka, V. I. Sidei, I. E. Barchii, S. V. Kun and A. V. Kun, Preparation, Stability Regions, and Properties of M2TeI6 (M=Rb, Cs, Tl) Crystals, *Inorg. Mater.*, 2002, **38**(8), 859–863.

32 L. Zhou, J.-F. Liao, Z.-G. Huang, X.-D. Wang, Y.-F. Xu, H.-Y. Chen, D.-B. Kuang and C.-Y. Su, All-Inorganic Lead-Free Cs2PdX6 (X=Br, I) Perovskite Nanocrystals with Single Unit Cell Thickness and High Stability, *ACS Energy Lett.*, 2018, **3**(10), 2613–2619.

33 A. Abfalterer, J. Shamsi, D. J. Kubicki, C. N. Savory, J. Xiao, G. Divitini, W. Li, S. Macpherson, K. Gałkowski, J. L. MacManus-Driscoll, D. O. Scanlon and S. D. Stranks, Colloidal Synthesis and Optical Properties of Perovskite-Inspired Cesium Zirconium Halide Nanocrystals, *ACS Mater. Lett.*, 2020, **2**(12), 1644–1652.

34 A. Wang, X. Yan, M. Zhang, S. Sun, M. Yang, W. Shen, X. Pan, P. Wang and Z. Deng, Controlled Synthesis of Lead-Free and Stable Perovskite Derivative Cs2SnI6 Nanocrystals via a Facile Hot-Injection Process, *Chem. Mater.*, 2016, **28**(22), 8132–8140.

35 Z. Tan, J. Li, C. Zhang, Z. Li, Q. Hu, Z. Xiao, T. Kamiya, H. Hosono, G. Niu, E. Lifshitz, Y. Cheng and J. Tang, Highly Efficient Blue-Emitting Bi-Doped Cs2SnCl6 Perovskite Variant: Photoluminescence Induced by Impurity Doping, *Adv. Funct. Mater.*, 2018, **28**(29), 1801131.

36 A. Yan, K. Li, Y. Zhou, Y. Ye, X. Zhao and C. Liu, Tuning the optical properties of Cs2SnCl6:Bi and Cs2SnCl6:Sb lead-free perovskites via post-annealing for white LEDs, *J. Alloys Compd.*, 2020, **822**, 153528.

37 J. Li, Z. Tan, M. Hu, C. Chen, J. Luo, S. Li, L. Gao, Z. Xiao, G. Niu and J. Tang, Antimony doped Cs2SnCl6 with bright and stable emission, *Front. Optoelectron.*, 2019, **12**(4), 352–364.

38 Z. Tan, Y. Chu, J. Chen, J. Li, G. Ji, G. Niu, L. Gao, Z. Xiao and J. Tang, Lead-Free Perovskite Variant Solid Solutions Cs2Sn1−xTexCl6: Bright Luminescence and High Anti-Water Stability, *Adv. Mater.*, 2020, **32**(32), 2002443.

39 R. Zeng, K. Bai, Q. Wei, T. Chang, J. Yan, B. Ke, J. Huang, L. Wang, W. Zhou, S. Cao, J. Zhao and B. Zou, Boosting triplet self-trapped exciton emission in Te(IV)-doped Cs2SnCl6 perovskite variants, *Nano Res.*, 2021, **14**(5), 1551–1558.

40 F. Locardi, E. Sartori, J. Buha, J. Zito, M. Prato, V. Pinchetti, M. L. Zaffalon, M. Ferretti, S. Brovelli, I. Infante, L. De Trizio and L. Manna, Emissive Bi-Doped Double Perovskite Cs2Ag1−xNaxInCl6 Nanocrystals, *ACS Energy Lett.*, 2019, **4**(8), 1976–1982.

41 C.-Y. Wang, P. Liang, R.-J. Xie, Y. Yao, P. Liu, Y. Yang, J. Hu, L. Shao, X. W. Sun, F. Kang and G. Wei, Highly Efficient Lead-Free (Bi,Ce)-Codoped Cs2Ag0.4Na0.6InCl6 Double Perovskites for White Light-Emitting Diodes, *Chem. Mater.*, 2020, **32**(18), 7814–7821.

42 B. Zhang, M. Wang, M. Ghini, A. E. M. Melcherts, J. Zito, L. Goldoni, I. Infante, M. Guizzardi, F. Scotognella, I. Kriegel, L. De Trizio and L. Manna, Colloidal Bi-Doped Cs2Ag1−xNaxInCl6 Nanocrystals: Undercoordinated Surface Cl Ions Limit their Light Emission Efficiency, *ACS Mater. Lett.*, 2020, **2**(11), 1442–1449.

43 H. Arfin, A. S. Kshirsagar, J. Kaur, B. Mondal, Z. Xia, S. Chakraborty and A. Nag, ns2 Electron (Bi3+ and Sb3+) Doping in Lead-Free Metal Halide Perovskite Derivatives, *Chem. Mater.*, 2020, **32**(24), 10255–10267.

44 Y. Jing, Y. Liu, X. Jiang, M. S. Molokeev, Z. Lin and Z. Xia, Sb3+ Dopant and Halogen Substitution Triggered Highly Efficient and Tunable Emission in Lead-Free Metal Halide Single Crystals, *Chem. Mater.*, 2020, **32**(12), 5327–5334.

45 H. Arfin, J. Kaur, T. Sheikh, S. Chakraborty and A. Nag, Bi 3+–Er 3+ and Bi 3+–Yb 3+ Codoped Cs 2 AgInCl 6 Double Perovskite Near–Infrared Emitters, *Angew. Chem.*, 2020, **132**(28), 11403–11407.

46 D. Zhu, M. L. Zaffalon, J. Zito, F. Cova, F. Meinardi, L. De Trizio, I. Infante, S. Brovelli and L. Manna, Sb-Doped Metal Halide Nanocrystals: A 0D versus 3D Comparison, *ACS Energy Lett.*, 2021, **6**(6), 2283–2292.

47 B. Zhou, Z. Liu, S. Fang, H. Zhong, B. Tian, Y. Wang, H. Li, H. Hu and Y. Shi, Efficient White Photoluminescence from Self-Trapped Excitons in Sb3+/Bi3+-Codoped Cs2NaInCl6 Double Perovskites with Tunable Dual-Emission, *ACS Energy Lett.*, 2021, **6**(9), 3343–3351.

48 L. R. V. Buizza, A. D. Wright, G. Longo, H. C. Sansom, C. Q. Xia, M. J. Rosseinsky, M. B. Johnston, H. J. Snaith and L. M. Herz, Charge-Carrier Mobility and Localization in Semiconducting Cu2AgBiI6 for Photovoltaic Applications, *ACS Energy Lett.*, 2021, **6**(5), 1729–1739.

49 R. S. Lamba, P. Basera, S. Singh, S. Bhattacharya and S. Sapra, Lead-Free Alloyed Double-Perovskite Nanocrystals of Cs2(NaxAg1−x)BiBr6 with Tunable Band Gap, *J. Phys. Chem. C*, 2021, **125**(3), 1954–1962.

50 S. J. Zelewski, J. M. Urban, A. Surrente, D. K. Maude, A. Kuc, L. Schade, R. D. Johnson, M. Dollmann, P. K. Nayak, H. J. Snaith, P. Radaelli, R. Kudrawiec, R. J. Nicholas, P. Plochocka and M. Baranowski, Revealing the nature of photoluminescence emission in the metal-halide double perovskite Cs2AgBiBr6, *J. Mater. Chem. C*, 2019, **7**(27), 8350–8356.

51 M. de Jong, L. Seijo, A. Meijerink and F. T. Rabouw, Resolving the ambiguity in the relation between Stokes shift and Huang–Rhys parameter, *Phys. Chem. Chem. Phys.*, 2015, **17**(26), 16959–16969.

52 Y. Jing, Y. Liu, J. Zhao and Z. Xia, Sb3+ Doping-Induced Triplet Self-Trapped Excitons Emission in Lead-Free Cs2SnCl6 Nanocrystals, *J. Phys. Chem. Lett.*, 2019, **10**(23), 7439–7444.

53 A. Dey, J. Ye, A. De, E. Debroye, S. K. Ha, E. Bladt, A. S. Kshirsagar, Z. Wang, J. Yin, Y. Wang, L. N. Quan, F. Yan, M. Gao, X. Li, J. Shamsi, T. Debnath, M. Cao, M. A. Scheel, S. Kumar, J. A. Steele, M. Gerhard, L. Chouhan, K. Xu, X.-g. Wu, Y. Li, Y. Zhang, A. Dutta, C. Han, I. Vincon, A. L. Rogach, A. Nag, A. Samanta, B. A. Korgel, C.-J. Shih, D. R. Gamelin, D. H. Son, H. Zeng, H. Zhong, H. Sun, H. V. Demir, I. G. Scheblykin, I. Mora-Seró, J. K. Stolarczyk, J. Z. Zhang, J. Feldmann, J. Hofkens, J. M. Luther, J. Pérez-Prieto, L. Li, L. Manna, M. I. Bodnarchuk, M. V. Kovalenko, M. B. J. Roeffaers, N. Pradhan, O. F. Mohammed, O. M. Bakr, P. Yang, P. Müller-Buschbaum, P. V. Kamat, Q. Bao, Q. Zhang, R. Krahne, R. E. Galian, S. D. Stranks, S. Bals, V. Biju, W. A. Tisdale, Y. Yan, R. L. Z. Hoye and L. Polavarapu, State of the Art and Prospects for Halide Perovskite Nanocrystals, *ACS Nano*, 2021, **15**(7), 10775–10981.

54 A. Dong, X. Ye, J. Chen, Y. Kang, T. Gordon, J. M. Kikkawa and C. B. Murray, A Generalized Ligand-Exchange Strategy Enabling Sequential Surface Functionalization of Colloidal Nanocrystals, *J. Am. Chem. Soc.*, 2011, **133**(4), 998–1006.

55 P. Giannozzi, S. Baroni, N. Bonini, M. Calandra, R. Car, C. Cavazzoni, D. Ceresoli, G. L. Chiarotti, M. Cococcioni, I. Dabo, A. Dal Corso, S. de Gironcoli, S. Fabris, G. Fratesi, R. Gebauer, U. Gerstmann, C. Gougoussis, A. Kokalj, M. Lazzeri, L. Martin-Samos, N. Marzari, F. Mauri, R. Mazzarello, S. Paolini, A. Pasquarello, L. Paulatto, C. Sbraccia, S. Scandolo, G. Sclauzero, A. P. Seitsonen, A. Smogunov, P. Umari and R. M. Wentzcovitch, QUANTUM ESPRESSO: a modular and open-source software project for quantum simulations of materials, *J. Phys.: Condens. Matter*, 2009, **21**(39), 395502.

56 J. P. Perdew, K. Burke and M. Ernzerhof, Generalized Gradient Approximation Made Simple, *Phys. Rev. Lett.*, 1996, **77**(18), 3865–3868.